

## N-induced Quantum Dots in GaAs/Ga(N, As) Core/Shell Nanowires: Symmetry, Strain, and Electronic Structure

M. Jansson,<sup>1</sup> F. Ishikawa,<sup>2</sup> W. M. Chen,<sup>1</sup> and I. A. Buyanova<sup>1,\*</sup>

<sup>1</sup>*Department of Physics, Chemistry and Biology, Linköping University, 58183 Linköping, Sweden*

<sup>2</sup>*Graduate School of Science and Engineering, Ehime University, 790-8577 Matsuyama, Japan*

(Received 29 June 2018; revised manuscript received 15 August 2018; published 16 October 2018; corrected 16 October 2020)

Nanowires (NWs) with embedded zero-dimensional (0D) quantum dots (QDs) have interesting fundamental properties attractive for a variety of applications. The properties of such embedded QDs can be controlled by 0D quantum confinement and also via strain engineering in axial or radial heterostructures of the nanowire system. We evaluate the electronic structure of QDs, which are formed in the Ga(N, As) shell of the GaAs/Ga(N, As) core-shell NWs due to alloy fluctuations. It is found that the principal quantization axis of the studied QDs is primarily oriented along the NW axis, based on the performed polarization-resolved magneto-photoluminescence measurements. We also show that the QDs exhibit a large spectrally dependent variation of the valence band character, which changes from pure heavy-hole states for the low-energy QD emitters to the mixed light-hole heavy-hole states for the QDs emitting at high energies. We ascribe these changes to combined effects of the uniaxial strain caused by the lattice mismatch between the GaAs core and the Ga(N, As) shell, and the local strain/lattice distortion within the short-range fluctuations in the N content. The obtained results underline the importance of the local strain for valence band engineering in hybrid NW structures with embedded QDs.

DOI: 10.1103/PhysRevApplied.10.044040

### I. INTRODUCTION

III-V semiconductor nanowires (NWs) with embedded zero-dimensional (0D) quantum dots (QDs) represent promising building blocks for future electronic and optoelectronic devices with advanced functionalities [1–10]. Utilizing the nanowire geometry relaxes lattice-matching constraints on substrate materials, which makes it possible to fabricate NWs on cheap foreign substrates, such as Si, advantageous for the integration of III-V optoelectronic nanodevices with Si-based microelectronics [11,12]. The NW architecture also provides freedom in heterostructure engineering via radial and axial designs [13,14]. Incorporating quantum structures in the NWs, such as quantum wells, quantum wires, and QDs, further extends flexibilities in controlling the electronic properties of such systems by utilizing quantum confinement effects. For example, using QDs in NWs allows complete quantum confinement, which is beneficial for realization of, e.g., nanolasers [10] or single photon light sources [3,7], where the embedded QD acts as a light emitter, whereas the NW provides an efficient cavity/waveguide, facilitating light extraction.

Several approaches for fabrication of such hybrid NW/QD structures have been exploited in the past. These include QD formation via (i) polytypism that

is characteristic for the III-V semiconductors in the NW geometry [2,9] and (ii) deliberate lateral confinement in axial heterostructures, i.e., by inserting a narrow layer of a low band gap semiconductor into a wide band gap NW matrix. The latter was demonstrated in, e.g., GaP/Ga(As<sub>x</sub>P<sub>1-x</sub>) [1], In(Ga)As/GaAs [10], In(As<sub>x</sub>P<sub>1-x</sub>)/InP [3,7], and GaAs/(Al<sub>x</sub>Ga<sub>1-x</sub>)As [8] material systems. In addition, it was found that in GaAs/(Al<sub>x</sub>Ga<sub>1-x</sub>)As NWs the QDs can be formed in the (Al<sub>x</sub>Ga<sub>1-x</sub>)As region due to variations in the Al content [6,15]. Independent of the specific mechanism for the QD formation, the majority of such hybrid NW/QD systems utilize heterostructure design and, therefore, often experience strain caused by lattice mismatch between the involved materials. This strain further alters the electronic properties of the embedded QDs providing a new degree of freedom in their design. For example, uniaxial/biaxial strain affects valence band (VB) states by modifying splitting between the light-hole (LH) and heavy-hole (HH) sub-bands. This may prove useful in, e.g., quantum computing applications, where the control of the hole states is vital [16–18]. For instance, whereas the HH ground state has been shown to have a longer spin coherence time, the LH ground state is preferable for electron-spin initialization [17]. The biaxial strain in the QDs formed in axial NW heterostructures ensures the HH character of the ground state, similar to the case of planar self-assembled QDs.

\*irb@ifm.liu.se

On the other hand, the ordering of the VB states may be significantly altered and even reversed when the QDs are embedded in the core/shell NW, where the strain that is created due to the lattice mismatch between the core and shell materials is uniaxial along the NW axis [19].

Recently, we have shown that the spontaneous QD formation is facilitated in NW heterostructures based on dilute nitride alloys, such as GaAs/Ga(N, As) core/shell NWs [20]. Here, the QDs are formed in the active Ga(N, As) shell due to short-range fluctuations in the N composition that enable carrier confinement due to the giant band gap bowing [21]: incorporation of only 1% of nitrogen in GaAs reduces the band gap energy by approximately 0.14 eV. This tunability of the band gap energy combined with other N-induced modifications of the electronic and material properties makes Ga(N, As) promising for applications as light emitters within the near-infrared spectral range [22,23], in third-generation photovoltaic devices [24,25], and also for room-temperature spin-functional devices [26–28]. Implementation of this material in NW/QD structures with high optical quality allows to combine these useful properties with advantages offered by the NW architecture. Dilute nitrides also have a rare feature in that the reduction of the band gap energy is accompanied with a decrease in their lattice constant, which should reverse the direction of strain in the formed QDs as compared with the conventional systems and may affect the character of the electronic states. An additional perturbation may be introduced because of local strain induced by changes of the lattice constant and/or local distortion within the QD regions. So far, however, the electronic structure of QDs spontaneously formed in the Ga(N, As)-based NWs is not understood. In this paper, we address this important issue and show that the hole character of the QDs embedded in GaAs/Ga(N, As) core/shell NWs is determined by combined effects of the strain due to the core-shell lattice mismatch and local crystal field within strongly localized states induced by local fluctuations in the N composition. As the result, the hole character in the formed QD emitters ranges from pure HH states for the low-energy emitters to states with strong LH-HH mixing for the high-energy ones.

## II. EXPERIMENT

The studied GaAs/Ga(N, As) core/shell NW structures are fabricated using plasma-assisted solid-source molecular beam epitaxy (MBE) on the (111) surface of silicon substrates using Ga droplets as a catalyst. The GaAs core is first grown using vapor-liquid-solid growth, on which the Ga(N, As) shell is formed via step-mediated growth—see Ref. [29] for a detailed description of the NW growth. Nitrogen composition in the Ga(N, As) shell is controlled by varying the N flux supplied from a N-plasma source and is estimated [30] as being 0.1% and 0.5%, based on a

detailed analysis of the temperature-dependent PL results within the framework of the band anticrossing model [31]. The performed scanning electron microscopy (SEM) and transmission electron microscopy (TEM) measurements show that the NWs have a uniform diameter of approximately 300 nm and are approximately 4- $\mu\text{m}$  long, on average. They have zincblende crystalline structure with minor wurtzite inclusions.

The samples are inserted into a LHe-cooled cryostat with a temperature range of 4–300 K, equipped with a superconducting magnet providing magnetic fields up to 5 T. The cryostat is fitted with a window for optical access, whereby  $\mu\text{PL}$  measurements can be performed in the backscattering geometry. The geometry of the setup is such that the excitation and detection paths always coincide with the axis of the magnetic field, which is directed perpendicular to the substrate. To perform magneto- $\mu\text{PL}$  spectroscopy on individual standing NWs, i.e., in the standing geometry, areas with a low NW density are first selected using SEM. Magneto- $\mu\text{PL}$  measurements in the lying geometry are done on NWs that are mechanically transferred onto another Si substrate. The PL emission is excited using a solid-state laser diode emitting at 660 nm. The excitation light is focused onto the sample to a spot of approximately 0.8–1  $\mu\text{m}$  using a 50X microscope objective ( $\text{NA} = 0.5$ ). The resulting PL is collected using the same objective lens and is detected by a single-grating monochromator combined with a Peltier-cooled Si-CCD detector. For linear (circular-) polarization-resolved PL measurements, a combination of a half-wave (quarter-wave) plate and a linear polarizer is used in front of the monochromator. All  $\mu\text{PL}$  measurements are performed at 5 K, unless otherwise stated.

## III. POLARIZATION-RESOLVED SPECTROSCOPY

Figures 1(a) and 1(b) provide an overview of  $\mu\text{PL}$  spectra acquired from single lying (i.e., transferred) GaAs/GaN<sub>0.001</sub>As<sub>0.999</sub> and GaAs/GaN<sub>0.005</sub>As<sub>0.995</sub> NWs, respectively. In addition to a broad background emission that stems [30] from radiative recombination of excitons weakly localized within long-range potential fluctuations in the Ga(N, As) shell, the spectra contain numerous sharp PL lines. We have previously shown that these lines originate from strongly-localized QD-like emitters within the Ga(N, As) shell with the principal quantization axis of the QDs preferentially aligned along the NW growth axis ( $z$ ) [20]. The weak emission observed at energies exceeding the Ga(N, As) band gap (approximately 1.4 eV for [N] = 0.5%) stems from the GaAs core [32] and will not be discussed further in this paper.

In the lying geometry, the majority of the sharp PL lines are linearly polarized perpendicular to the NW axis. This is demonstrated in the insets in Figs. 1(a) and 1(b), where

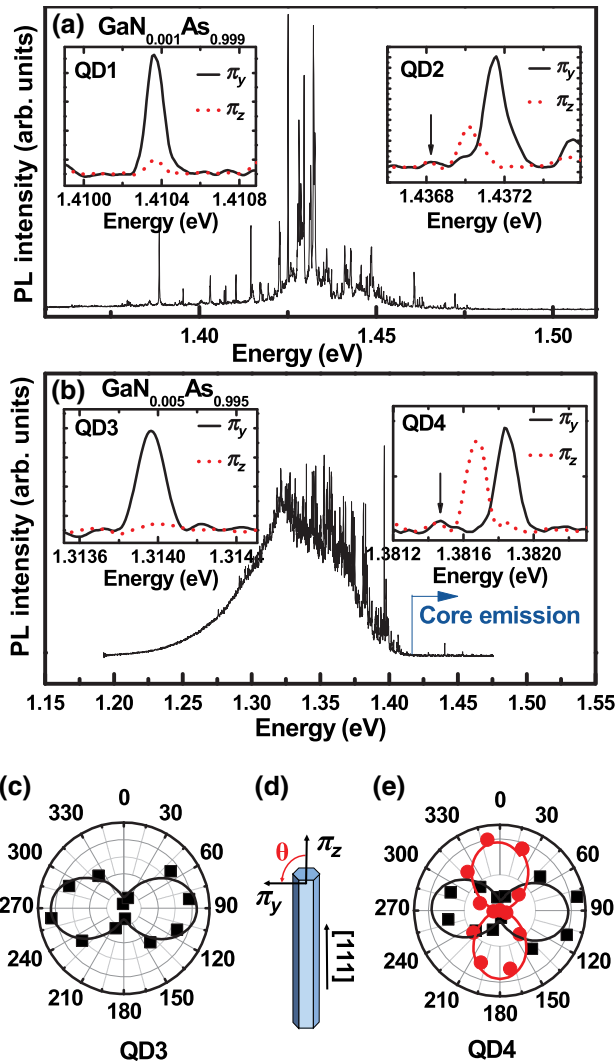


FIG. 1. PL spectra measured at 5 K from single GaAs/GaN<sub>0.001</sub>As<sub>0.999</sub> (a) and GaAs/GaN<sub>0.005</sub>As<sub>0.995</sub> (b) core/shell NWs. The insets show polarization-resolved PL spectra from representative type-A and type-B QDs emitting at low and high energies, respectively. The emission from the type-A QDs is comprised of a single line that is linearly polarized along the NW axis, whereas the type-B QDs emit two bright, orthogonally polarized lines and a much weaker line at the lower energy. (c) and (e) are polar plots from the polarization-resolved PL measurements from QD3 and QD4, respectively, where the red circles (black squares) represent the PL intensities of the  $\pi_z$  ( $\pi_y$ ) polarized components. (d) defines the polarization angle,  $\theta$ , with respect to the NW axis.

polarization-resolved spectra representative for the high- and low-energy QD lines are shown. From a close examination of the spectra, it is noticeable that the fine structure of the QD emission varies significantly. The emission from the low-energy emitters (labeled QD1 and QD3) consists of a single line that is linearly polarized in the  $y$  direction, i.e., orthogonal to the NW axis. Such QDs will be

referred to below as type-A QDs. On the other hand, the high-energy emission (QD2 and QD4) consists of three components for each emitter: two bright, orthogonally polarized lines and a much weaker line at the lower energy (indicated by the arrows in the figures). We denote such QDs as type-B QDs. The polarization-resolved PL intensity of the two dominating lines of QD4 is displayed as the polar plot in Fig. 1(e), while Fig. 1(c) shows the corresponding polar plot of the single line from QD3. The angle  $\theta$  in the plots is 0 (90) degrees for detection of light linearly polarized parallel (orthogonal) to the direction of the NW axis ( $z$ )—see Fig. 1(d). All PL lines have a high degree of polarization (>90%).

Due to the large NW diameter, contributions of the so-called antenna effect due to dielectric mismatch between the NW and its surroundings [33–35] can be neglected in the studied wires. Therefore, the polarization properties of the different states are governed by the hole character of the exciton [36–42]. In the geometry of lying NWs, with excitation and detection along the  $x$  direction, both the  $y$  and  $z$  components of the emitted light are detectable. A pure HH exciton has two bright  $| \pm 1 \rangle$  states, which are degenerate in a high-symmetry QD ( $C_{3v}$  or higher) emitting circularly polarized light—see also Supplemental Material [43], Sec. S1 for an in-depth discussion of the exciton states. (The notation is given in the  $|M\rangle$  basis, where  $M$  is the quantum number representing the  $z$  projection of the total angular momentum of the exciton.) For the QDs with their principal quantization axes aligned along the  $z$  direction, light with the electric-field vector in the  $x$ - $y$  plane, which is circularly polarized along the  $z$  direction, will be detected as being linearly  $\pi_y$  polarized in the given measurement geometry. This is seen for QD1 and QD3, implying that the low-energy excitons are of pure HH character and the preferential quantization axis of the QD is directed along the NW axis. As the QD2 and QD4 spectra contain also a  $\pi_z$  polarized line, they clearly do not originate from pure HH excitons. The appearance of this  $\pi_z$  polarized line suggests some degree of LH-HH mixing, resulting in the recombination from the  $|1,0\rangle$  state. (To describe states with LH-HH mixing, both the  $J$  and  $M$  quantum numbers are needed, and the  $|J,M\rangle$  basis is used.) We note that the appearance of both types of QDs does not correlate with the presence of twins or wurtzite inclusions in the NWs, as shown in the Supplemental Material [43], Sec. S3.

#### IV. MAGNETO-OPTICAL SPECTROSCOPY

To gain further understanding of the electronic structure of the revealed QD emitters, magneto-optical spectroscopy is performed on single NWs, either lying (i.e., for the transferred NWs) or standing, as illustrated on the top of Fig. 2. Due to restrictions in the geometry of the setup, it is not possible to investigate the same NW in both geometries. The data from the lying and standing NWs are thus

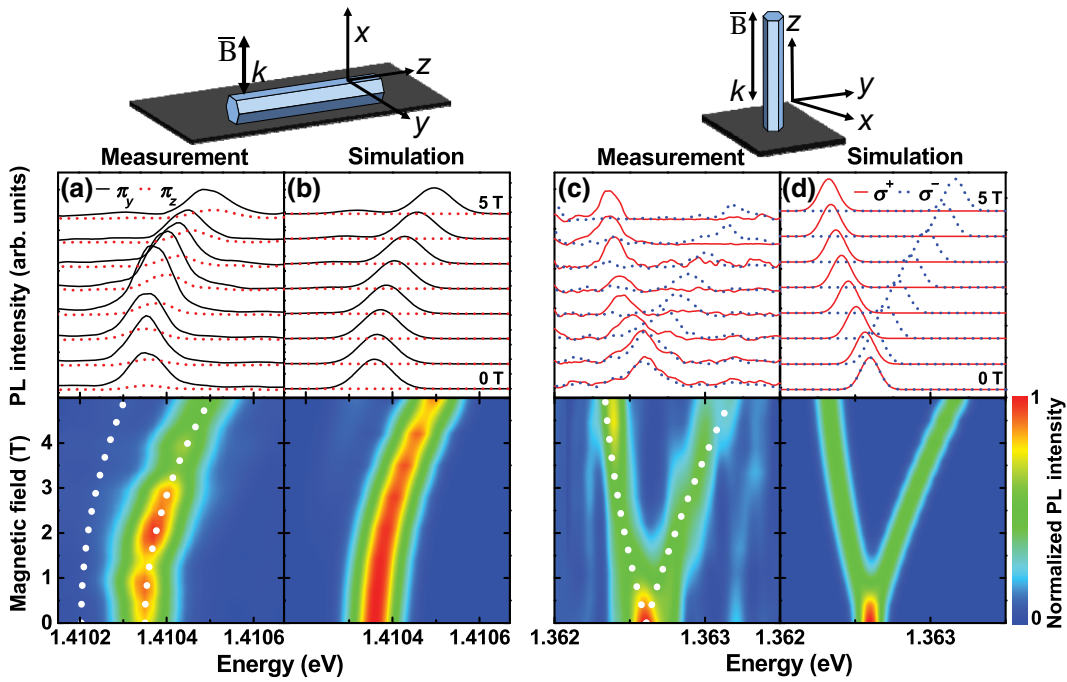


FIG. 2. Polarization-resolved  $\mu$ PL spectra (the upper part) and color plots (the lower part) of the total PL intensity from the type-A QDs embedded in a single  $\text{GaN}_{0.001}\text{As}_{0.999}$  NW, measured under an applied magnetic field in the lying (a) and standing (c) geometries. (b) and (d) show the corresponding simulated PL spectra and color plots, where the PL intensity scales with the calculated oscillator strength and the line widths are taken from the measurement data. The dotted white lines in (a) and (c) represent the eigenvalues deduced from the simulations. The spectra within the upper parts of the figure are vertically offset for clarity.  $\mathbf{B}$  and  $\mathbf{k}$  denote the magnetic field and light propagation direction with respect to the coordinate frame of the NW.

acquired from different NWs and, therefore, from different QDs. To allow a comparison between the two geometries, the properties of the two QDs are assumed to be similar, as supported by the fact that most of the studied QDs emitting within the same energy range display similar Zeeman patterns.

### A. Electronic structure of type-A low-energy emitters

We first discuss results from the magneto-optical measurements of the low-energy emitters. Figures 2(a) and 2(c) show the corresponding polarization-resolved  $\mu$ PL spectra and color plots of the total PL intensity acquired in the geometries of lying and standing NWs, respectively, taking as an example the  $\text{GaAs}/\text{GaN}_{0.001}\text{As}_{0.999}$  NW structure. (The experimental data from the  $\text{GaAs}/\text{GaN}_{0.005}\text{As}_{0.995}$  NWs can be found in the Supplemental Material [43], Sec. S4.) In both geometries, the zero-field spectra contain a single line. In the lying geometry ( $\mathbf{B} \parallel \mathbf{k} \parallel x$ ), this line shows no splitting in applied magnetic fields  $\mathbf{B}$ , but a weak low-energy component appears at around  $\mathbf{B} = 4$  T. In the standing geometry ( $\mathbf{B} \parallel \mathbf{k} \parallel z$ ), splitting into two circularly polarized components is observed. This behavior of the type-A QDs supports our assumption that the detected PL emission is due to recombination of the HH exciton. In the standing geometry, the splitting between the bright

$|\pm 1\rangle$  states gives rise to the two circularly polarized PL components. Since the PL linewidth is very similar at 0 and 5 T, the two bright states should be nearly degenerate at zero field, which implies  $C_{3v}$  or higher symmetry of the QDs. The higher intensity of the low-energy PL component with  $\sigma^-$  polarization is attributed to thermalization between the two  $|\pm 1\rangle$  sublevels, which should favor the low-energy  $| -1 \rangle$  one. With the magnetic field directed along the  $x$  axis in the lying geometry, we expect symmetry lowering and thereby admixing of the bright  $|\pm 1\rangle$  states, resulting in the  $|1_x\rangle$  and  $|1_y\rangle$  states that emit light linearly polarized in the corresponding directions. (Here,  $|M_{x/y}\rangle$  is defined as  $|M\rangle \mp | -M\rangle$ .) Consequently, only the  $|1_y\rangle$  state should be visible in the experimental geometry at a given magnetic field. The dark  $|\pm 2\rangle$  states are expected to be mixed even at zero field in symmetries lower than  $C_{3v}$ . In applied magnetic fields along the  $x$  axis, they also acquire a projection on the bright  $|1_x\rangle$  and  $|1_y\rangle$  states, making them partially bright. The emission from these states will also be polarized in the  $x$  and  $y$  directions, respectively, making only one of the lines detectable in the measurement geometry. The lower-energy component in Fig. 2(a) is thus ascribed to one of the dark  $|\pm 2\rangle$  states. This qualitative analysis is confirmed by our simulations performed for the HH exciton using the spin Hamiltonian that takes into account the exchange interaction between the electron

and hole, as well as strain and an applied magnetic field, as described in Supplemental Material [43], Sec. S1. The corresponding results are shown in Figs. 2(b) and 2(d) for the lying and standing geometries, respectively, and are in agreement with the experimental data. The eigenenergies of the bright and partially bright states that are found from the best fit of the spin Hamiltonian to the experimental data are shown by the white dotted lines in Figs. 2(a) and 2(c). From the results acquired in the two measurement geometries, we can determine  $\delta_0 = 130 \mu\text{eV}$  and  $\delta_1 \sim 10 \mu\text{eV}$ , where  $\delta_0$  and  $\delta_1$  are the zero-field splitting between the bright and dark states and the anisotropic exchange splitting between the bright states, respectively. The electronic structure of the exciton in the QDs is schematically illustrated in Fig. S1 of Supplemental Material [43]. Since we can only detect one of the two  $|\pm 2\rangle$  states, the  $\delta_2$  parameter that characterizes their zero-field splitting cannot be determined. The analysis also yields values of the diamagnetic shift ( $\gamma$ ) and the exciton Landé g-factors:  $\gamma_x = 4.5 \mu\text{eV}/\text{T}^2$ ,  $\gamma_z = 5.8 \mu\text{eV}/\text{T}^2$ ,  $g_X^x = 0.4$ , and  $g_X^z = 2.9$ .

The results obtained from different type-A emitters are summarized in Table I.  $\delta_0$  is found to be generally larger than  $\delta_1$ , which is characteristic for the HH exciton in QDs [44–47]. The results also indicate that  $\delta_1$  is typically small for  $\text{GaN}_{0.001}\text{As}_{0.999}$  NWs, i.e., of the order of 10–100  $\mu\text{eV}$ , which implies a rather high symmetry of the formed dots. This is because for the ideal QDs grown on (111) or (001) planes with the symmetry of  $C_{3v}$  or  $D_{2d}$ , respectively, no anisotropic exchange splitting is expected, i.e.,  $\delta_1 = 0$ . In

practice, however, even for self-assembled QDs grown on (001) substrates, a large variation of  $\delta_1$  is reported, with  $\delta_1$  being as large as 1 meV in  $\text{In}(\text{Ga})\text{As}$ - and  $(\text{Al}_x\text{Ga}_{1-x})\text{As}$ -based QDs [46–52]. This is usually attributed to a lowering of the QD symmetry due to shape/strain anisotropy or in-plane piezoelectric fields. It has, however, been predicted [53] and experimentally shown [54–56] that such effects are reduced for QDs grown on the (111) surface, leading to a significantly smaller or even vanishing  $\delta_1$ . The same seems to be true for the studied QDs embedded in the NWs of which the principal quantization axis is along the NW axis (i.e., (111)). We note that the QD anisotropy seems to be slightly more pronounced when the nitrogen composition is increased to 0.5%—see Table I.

## B. Electronic structure of type-B high-energy emitters

Let us now discuss the electronic structure of the high-energy QDs, referred to below as type-B QDs. Figure 3 shows evolution of the PL spectra from representative type-B emitters measured in the lying (a) and standing (c) geometries. The zero-field PL spectrum in the lying geometry [Fig. 3(a)] contains a pair of lines that are separated by 130  $\mu\text{eV}$  and have strong  $\pi_z$  and  $\pi_y$  polarization, respectively, accompanied by a weak feature at the lower energy. (The weak lines above 1.4375 eV are believed to originate from a different emitter and are not included in the analysis.) In an applied magnetic field, the bright pair of lines shows a strong Zeeman splitting and depolarization, which

TABLE I. Exchange and magnetic field fitting parameters for the type-A QDs. Due to the selection rules for optical transitions, the  $\delta_0$  ( $\delta_1$ ) parameters can be deduced only in the lying (standing) geometry.

Sample	Measurement geometry	Emission energy (eV)	$\delta_0$ ( $\mu\text{eV}$ )	$\delta_1$ ( $\mu\text{eV}$ )	$g_X^x$	$g_X^z$	$\gamma$ ( $\mu\text{eV}/\text{T}^2$ )
$\text{GaN}_{0.001}\text{As}_{0.999}$	Lying	1.395	277		0.2		6.9
$\text{GaN}_{0.001}\text{As}_{0.999}$	Lying	1.410		No new line with B			5.6
$\text{GaN}_{0.001}\text{As}_{0.999}$	Lying	1.410	130		0.4		4.5
$\text{GaN}_{0.001}\text{As}_{0.999}$	Lying	1.427		No new line with B			6.4
$\text{GaN}_{0.001}\text{As}_{0.999}$	Standing	1.363			7	2.9	5.8
$\text{GaN}_{0.001}\text{As}_{0.999}$	Standing	1.365			96	1.7	4.9
$\text{GaN}_{0.001}\text{As}_{0.999}$	Standing	1.367			10	2.3	2.9
$\text{GaN}_{0.001}\text{As}_{0.999}$	Standing	1.374			1	1.5	4.0
$\text{GaN}_{0.001}\text{As}_{0.999}$	Standing	1.416			71	0.7	5.6
$\text{GaN}_{0.005}\text{As}_{0.995}$	Lying	1.272		No new line with B			4.1
$\text{GaN}_{0.005}\text{As}_{0.995}$	Lying	1.278		No new line with B			4.3
$\text{GaN}_{0.005}\text{As}_{0.995}$	Lying	1.302	406		0.3		3.0
$\text{GaN}_{0.005}\text{As}_{0.995}$	Lying	1.314		No new line with B			4.3
$\text{GaN}_{0.005}\text{As}_{0.995}$	Lying	1.368		No new line with B			2.9
$\text{GaN}_{0.005}\text{As}_{0.995}$	Standing	1.333			11	0.5	2.0
$\text{GaN}_{0.005}\text{As}_{0.995}$	Standing	1.336			26	0.5	3.8
$\text{GaN}_{0.005}\text{As}_{0.995}$	Standing	1.337			5	0.7	3.8
$\text{GaN}_{0.005}\text{As}_{0.995}$	Standing	1.343			11	0.4	3.5
$\text{GaN}_{0.005}\text{As}_{0.995}$	Standing	1.347			18	0.5	3.4
$\text{GaN}_{0.005}\text{As}_{0.995}$	Standing	1.349			0	0.4	3.3
$\text{GaN}_{0.005}\text{As}_{0.995}$	Standing	1.363			36	2.2	2.6
$\text{GaN}_{0.005}\text{As}_{0.995}$	Standing	1.380			116	1.2	3.9

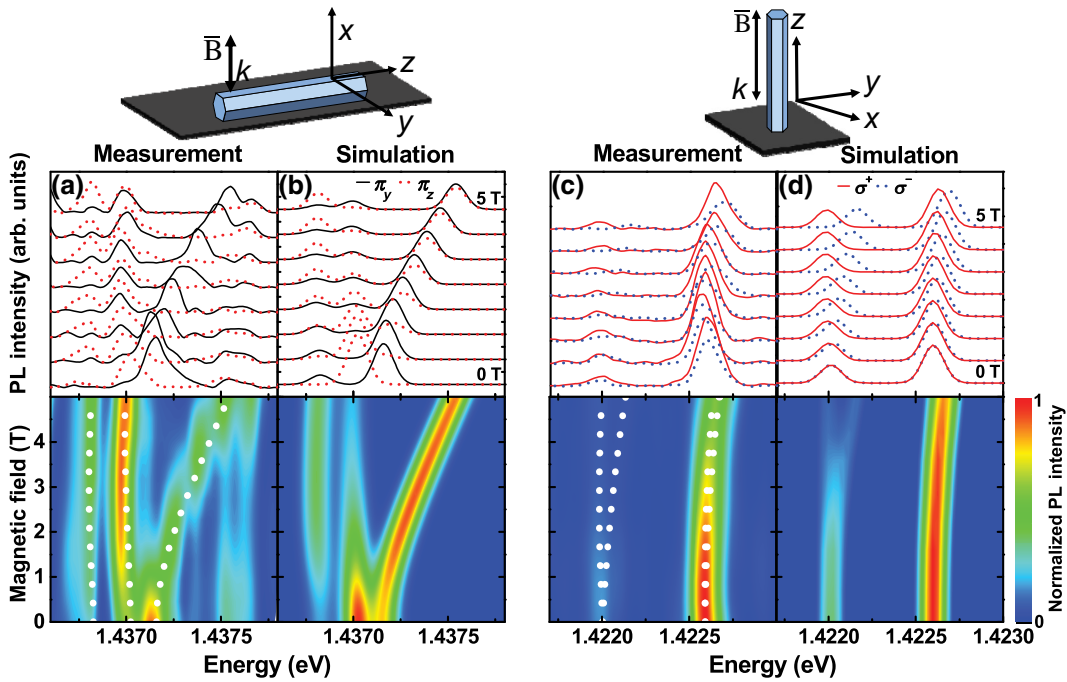


FIG. 3. Polarization-resolved  $\mu$ PL spectra (the upper part) and color plots (the lower part) of the total PL intensity from the type-B QDs embedded in a single  $\text{GaN}_{0.001}\text{As}_{0.999}$  NW, measured under an applied magnetic field in the lying (a) and standing (c) geometries. (b) and (d) show the corresponding simulated PL spectra and color plots, where the PL intensity scales with the calculated oscillator strength and the line width are taken from the measurement data. The dotted white lines in (a) and (c) represent the eigenvalues deduced from the simulations. The spectra within the upper parts of the figure are vertically offset for clarity.  $\mathbf{B}$  and  $\mathbf{k}$  denote the magnetic field and light propagation direction with respect to the coordinate frame of the NW.

is more severe for the  $\pi_z$  polarized line that completely loses its polarization at 5 T. The weak low-energy line dramatically increases in intensity with increasing magnetic field and acquires strong  $\pi_z$  polarization at 5 T. In the standing geometry, the zero-field PL spectrum contains two lines with the higher-energy one dominating in intensity. Upon applying a magnetic field, each of the two lines shows a weak Zeeman splitting into two circularly polarized components. The observed behavior of the type-B emitter is inconsistent with the pure HH transition discussed above and can only be explained if the valence band states have some admixture of the LH character. When the strain-induced LH-HH splitting is reduced, the electronic structure of the exciton will be dominated by the exchange interaction, which separates the bright triplet from the dark quintet states and also partially lifts the degeneracy of the states, as shown in Fig. S1 in the Supplemental Material [43]. If the exchange interaction is small enough, however, there will be some mixing of the bright and dark states even for QDs with high symmetry, such as  $C_{3v}$ , and the following two dark states will become partially allowed:  $\psi_1 = a|2,1\rangle - b|1,1\rangle$  and  $\psi_2 = a|2,-1\rangle + b|1,-1\rangle$ . Here, the normalization factors obey  $a > b$ . As these “partially bright” states are formed from the “dark” quintuplet, they will appear at lower energies than the bright triplet states. In the standing geometry, an applied magnetic field will

lift the remaining degeneracy but preserve the character of the states. In the geometry of the experiment, one would, therefore, expect two sets of circularly polarized components with the higher (lower) energy set originating from the bright (partially bright) states. In the lying geometry, an applied magnetic field will break the isotropy between the  $x$  and  $y$  directions and mix the states as:  $\psi_1 = a(|2,-1\rangle + |2,1\rangle) + b(|1,-1\rangle - |1,1\rangle)$  and  $\psi_2 = a(|2,-1\rangle - |2,1\rangle) + b(|1,-1\rangle + |1,1\rangle)$ , leading to linear polarization of the light. The  $\psi_1$  ( $\psi_2$ ) state may further obtain a projection along the  $|2,0\rangle$  ( $|1,0\rangle$ ) state, leading to  $\pi_z$  polarized emission from  $\psi_2$ . The initially dark states at low energy are thus attributed to the  $\psi_2$  and the degenerate  $\psi_1$  and  $\psi_2$  states in the lying and standing geometries, respectively.

For type-B QDs with LH-HH mixing, we cannot assign a single exciton  $g$  value to describe the behavior in applied magnetic fields. Instead we must use the full  $8 \times 8$  spin Hamiltonian (see Supplemental Material [43], Sec. S1). In the Zeeman term of the spin Hamiltonian, the parameters  $K$  and  $L$  are now assumed to be different from those described by Luttinger [57] for free excitons due to the confinement potential of the QD, and are used as fitting parameters. The best fit to the experimental data shown in Fig. 3a (3c) in the lying (standing) geometries is obtained when  $g_e = 0.7$  (1.0),  $K = -0.1$  (-0.5), and  $L = 0.6$  (0.4),

TABLE II. Exchange and magnetic field fitting parameters for the type-B QDs. Due to the selection rules for optical transitions, the complete set of exchange parameters can be deduced only in the lying geometry. In the standing geometry, the  $a_x$  and  $a_y$  parameters are arbitrarily set to zero, letting the  $a_z$  parameter fully account for the splitting between the bright and partially bright states.

Sample	Measurement geometry	Emission energy (eV)	$a_z(\mu\text{eV})$	$a_x = a_y(\mu\text{eV})$	$g_e$	$K$	$L$	$\gamma(\mu\text{eV}/\text{T}^2)$
GaN <sub>0.001</sub> As <sub>0.999</sub>	Lying	1.437	330	30	0.7	-0.1	0.6	2.0
GaN <sub>0.001</sub> As <sub>0.999</sub>	Lying	1.469	200	-50	1.9	-0.2	0.3	7.9
GaN <sub>0.001</sub> As <sub>0.999</sub>	Standing	1.423	290		1.0	-0.5	0.4	2.5
GaN <sub>0.001</sub> As <sub>0.999</sub>	Standing	1.434	240		1.2	-0.4	0.4	2.4
GaN <sub>0.001</sub> As <sub>0.999</sub>	Standing	1.435	260		0.5	-0.5	0.3	8.1
GaN <sub>0.005</sub> As <sub>0.995</sub>	Lying	1.382	250	-40	0.6	-1.2	0.9	1.9
GaN <sub>0.005</sub> As <sub>0.995</sub>	Lying	1.381	340	-70	1.5	-0.9	0.4	1.0
GaN <sub>0.005</sub> As <sub>0.995</sub>	Standing	1.382	195		1.1	-1.1	0.6	2.0
GaN <sub>0.005</sub> As <sub>0.995</sub>	Standing	1.387	290		0.7	-1.0	0.5	1.2

where  $g_e$  is the electron  $g$  value. The zero-field exchange splitting between the bright states is found to be very close to zero, again confirming the high symmetry of the dots. The corresponding simulated PL spectra are displayed in Figs. 3(b) and 3(d), and the eigenenergies of the optically active states are shown by the white dotted lines in Figs. 3(a) and 3(c). The agreement between the experiment and simulation is observed, justifying the validity of the model. We note that ideally, the  $K$  and  $L$  parameters should be identical in the two geometries, but as the data in the two geometries are acquired from two different QDs, some variation is expected. The deduced parameters for different type-B QDs are summarized in Table II. First, we notice that the isotropic exchange interaction dominates along the  $z$  direction, which suggests that the main quantization axis of the formed QDs is directed along the NW axis. Secondly, the  $K$  parameter ranging from -0.5 to -0.1 in the QDs embedded in the GaN<sub>0.001</sub>As<sub>0.999</sub> NWs is quite close to that for the free exciton in GaAs (-0.5). In the GaN<sub>0.005</sub>As<sub>0.995</sub> NWs, on the other hand, the  $K$  parameter covers the range from -1.5 to -0.9. The latter implies that the hole becomes more localized with increasing N composition in Ga(N, As). Since the QDs are formed due to local fluctuations of the nitrogen composition, the confining potential should be primarily imposed on the electron, as N incorporation causes a dramatic down-shift of the conduction band (CB) edge [21]. In contrast, the VB states experience only a weak bowing in energy, which makes hole confinement probable only in the QDs with a relatively high N composition. Finally, the electron  $g$  factor is found to be isotropic, as the best fits to the data in both geometries yield very similar values (see also Table II). The determined electron  $g$  values (0.5–1.5) are similar to those reported previously in Ga(N, As) alloys with comparable N compositions [58].

### C. Exciton confinement

We now compare diamagnetic coefficients,  $\gamma$ , determined for the QDs emitting at various energies—see

Figs. 4(a) and 4(b). The corresponding values in the  $x$  and  $z$  directions are shown by the red filled circles and the orange open circles, respectively, for the QDs embedded in the GaN<sub>0.001</sub>As<sub>0.999</sub> (a) and GaN<sub>0.005</sub>As<sub>0.995</sub> (b) NW structures. From Fig. 4, the following trends can be distinguished. First, the average longitudinal values,  $\gamma_z$ , are found to be slightly smaller than the transverse ones,  $\gamma_x$ . For a strongly confined exciton, the diamagnetic coefficient is known to depend on the effective masses and localization of the wavefunction for the electron and hole, according to the equation [59]

$$\gamma = \frac{e^2}{8} \left( \frac{\langle r_e^2 \rangle}{m_e} + \frac{\langle r_h^2 \rangle}{m_h} \right). \quad (1)$$

Here,  $\langle r_{e/h} \rangle$  denotes the distribution of the electron/hole wavefunction, whereas  $m_e$  ( $m_h$ ) is the electron (hole) effective mass. Different diamagnetic shifts in the  $x$  and  $z$  directions thus imply that the exciton confinement is slightly stronger in the  $z$  direction than in the  $x$  direction, which supports the preferential alignment of the QD quantization axis along the NW axis. Second, the diamagnetic coefficients for the QDs embedded in the GaN<sub>0.001</sub>As<sub>0.999</sub> NWs are significantly larger than those in the GaN<sub>0.005</sub>As<sub>0.995</sub> NWs. This can be well accounted for by the drastic change in the electron effective mass upon alloying GaAs with nitrogen. Indeed, previous studies of Ga(N, As) epilayers have shown that  $m_e$  increases from approximately 0.09  $m_0$  to 0.15  $m_0$  when the nitrogen content changes from 0.1% to 0.5% [60]. Using these values of electron effective mass and assuming that the hole effective mass does not change upon nitrogen incorporation, we can compute an approximate size of the QD confinement potential. The values are obtained under a further simplified assumption that  $\langle r_e^2 \rangle \approx \langle r_h^2 \rangle \equiv \langle r^2 \rangle$ , and taking  $m_h = 0.51 m_0$  for the type-A QDs with the pure HH character and 0.30  $m_0$  (which is the average of the LH and HH effective masses in GaAs) for the type-B QDs with the mixed LH-HH character. The QD radius,  $r$ , is estimated using Eq. (1) as  $r = 2\sqrt{\langle r^2 \rangle}$

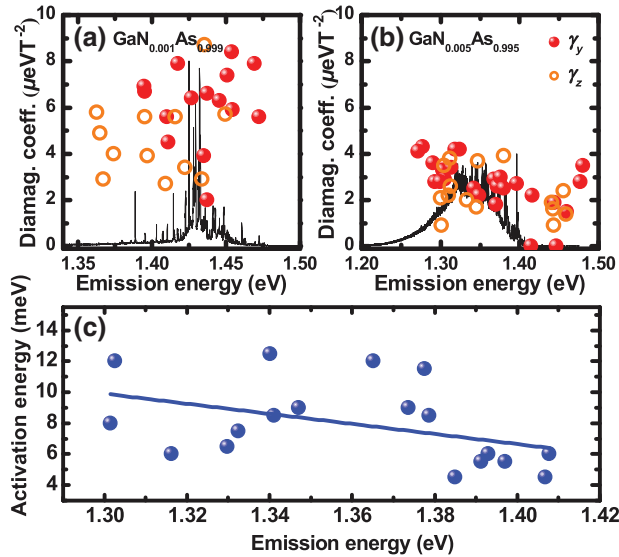


FIG. 4. Diamagnetic shift coefficients for various QDs embedded in the  $\text{GaN}_{0.001}\text{As}_{0.999}$  (a) and  $\text{GaN}_{0.005}\text{As}_{0.995}$  (b) NW structures. The red dots (orange open circles) show the diamagnetic coefficients in the  $y$  ( $z$ ) direction. For easy reference, typical PL spectra from the corresponding NWs are shown. We note that the shown parameters are the summary from several individual NWs of the same structure. (c) Thermal activation energies deduced from PL intensity quenching from several QDs embedded in the  $\text{GaN}_{0.005}\text{As}_{0.995}$  NW structure.

[61,62]. For the  $\text{GaN}_{0.001}\text{As}_{0.999}$  sample, such an estimate yields the out-of-plane radius  $r_{yz} = 8.7 \pm 1.4$  ( $9.3 \pm 0.7$ ) nm for the type-A (type-B) QDs, while the in-plane radius is  $r_{xy} = 7.9 \pm 0.9$  ( $7.8 \pm 1.8$ ) nm. The corresponding radii for the type-A (type-B) QDs in the  $\text{GaN}_{0.005}\text{As}_{0.995}$  sample are  $r_{yz} = 8.5 \pm 0.8$  ( $6.2 \pm 1.5$ ) nm and  $r_{xy} = 7.1 \pm 1.2$  ( $6.5 \pm 1.4$ ) nm. These values are comparable to those reported for the QDs formed in  $\text{Ga}(N,\text{As})$  epilayers due to alloy fluctuations, i.e., 6–8 nm for  $\text{Ga}(N,\text{As})$  with  $[\text{N}] = 1\%$  [63,64].

Further information regarding the exciton confinement within the revealed QDs is obtained from temperature-dependent  $\mu$ PL spectroscopy. It is found that the QD emissions experience quenching in intensity at elevated temperatures. Figure 4(c) shows thermal activation energies obtained for individual QD emissions from Arrhenius plots of their intensities, as also described in Supplemental Material [43], Sec. S5. The solid line in Fig. 4(c) represents a linear fit to the data (dots). On average, the activation energy is found to be higher for the low-energy emitters, though the deduced values scatter significantly between different QDs even with similar exciton energies. The observed trend is consistent with our suggestion that the low-energy emitters have, on average, a higher nitrogen composition and a larger size, since the former increases the depth of the confining potential while the

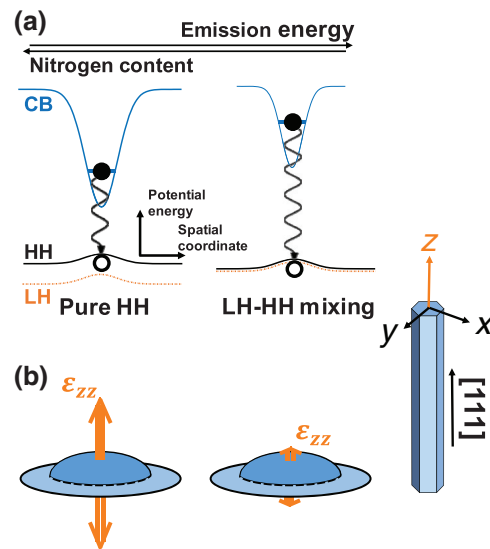


FIG. 5. (a) A schematic illustration of the energy diagrams of the investigated QDs, where the energies of the LH (HH) VB states are shown by the orange dotted (black solid) lines. The confinement energy is exaggerated relative to the total emission energy for easy viewing. The QD size is reflected by the width of the confinement potential. The strain acting within the QD, which is primarily responsible for the LH-HH splitting seen in (a), is represented by the arrows in (b). As the strain is thought to be dominated by a uniaxial component along the NW axis, the other components (e.g., the hydrostatic strain) are neglected in the figure.

latter decreases the QD confinement energy relative to the band gap.

## V. MECHANISM FOR THE QUANTUM DOT FORMATION

The suggested mechanism for the QD formation is illustrated in Fig. 5(a). The short-range potential fluctuations in the N content induce a 3D-confining potential for electrons, forming the QD states. The type-A QDs have, on average, a higher N composition and a weaker degree of the exciton confinement. They also experience a large splitting between the HH and LH VB states, which diminishes for the high-energy type-B emitters, to account for the magneto-PL data (Figs. 2 and 3). Because of the weak perturbation of the VB states upon N incorporation, the substantial LH-HH splitting for the low-energy emitters cannot be explained merely through a stronger confinement of the hole. Instead, we need to consider the effects of N-induced strain on the VB states, as the lattice constant of  $\text{Ga}(N,\text{As})$  decreases with increasing [N].

Strain in lattice-mismatched core/shell NWs has been thoroughly studied both theoretically [65] and experimentally [66,67], with the general conclusion that the induced strain can be decomposed into hydrostatic and uniaxial parts, where the uniaxial component ( $\epsilon_{zz}$ ) is along the NW

axis. The reduction of the lattice constant in the Ga(N, As) shell will induce a uniaxial tensile strain in this region, lifting the LH-HH degeneracy and leaving the HH states as the ground state. The hydrostatic part does not influence the state ordering. The uniaxial component of the strain can be calculated from the lattice mismatch of the core and shell materials of the NW using the Lamé-Clapeyron-Navier equation while accounting for the symmetry of a [111]-grown zincblende NW, following formalism developed in Ref. [65]. Assuming that the stiffness is uniform in the core and shell regions (i.e., that the effect of nitrogen incorporation on the elastic constants is negligible), the longitudinal (uniaxial) strain component in the shell is simply given by

$$\varepsilon_{zz} = -\eta f, \quad (2)$$

where  $\eta$  is the ratio between the core and full NW cross-section areas, while  $f$  is the lattice mismatch,  $f = (a_s - a_c)/a_c$ , between the core ( $c$ ) and shell ( $s$ ). The in-plane strain components are given in cylindrical coordinates by

$$\begin{aligned} \frac{\varepsilon_{\theta\theta} - \varepsilon_{rr}}{2} &= B_s \frac{r_c^2}{r^2} \\ \frac{\varepsilon_{\theta\theta} + \varepsilon_{rr}}{2} &= -\eta(f - B_s), \end{aligned} \quad (3)$$

where  $B_s$  is given by the elastic constants

$$B_s = -f \frac{c_{11} + 2c_{12}}{c_{11} + c_{12} + 2c_{44}}. \quad (4)$$

The in-plane warping term introduced in zincblende NWs grown in the [111] direction is ignored, as it is much smaller than the other in-plane strain components mentioned above [65]. The ratio  $\eta$  is estimated to be  $\eta = 0.11$  for the investigated structures, while the lattice mismatch,  $f$ , is composition-dependent and is computed using the following expressions for the core ( $c$ ) and shell ( $s$ ) lattice constants

$$\begin{aligned} a_c &= a_{\text{GaAs}} \\ a_s &= (1 - x)a_{\text{GaAs}} + x a_{\text{GaN}}. \end{aligned} \quad (5)$$

Here, Vegard's rule is used to compute the shell lattice constant as a function of the  $[\text{N}]/([\text{As}] + [\text{N}])$  fraction,  $x$ . By using the elastic constants for GaAs [68], the strain components in the core and shell can be calculated as a function of  $x$ . It is found that the shell strain is tensile, and the longitudinal component dominates over the in-plane one by approximately five times. For  $[\text{N}] = 0.1\%$ , the longitudinal strain component is computed to 0.002%, whereas for  $[\text{N}] = 0.5\%$  nitrogen, the strain component increases to 0.011%. This leads to a HH-LH splitting, which in magnitude is comparable to the exchange interaction and is, thus,

too small to ensure the pure HH character of the ground state. (See also Supplemental Material [43], Sec. S2.)

Therefore, to account for the observed pure HH character of the low-energy type-A QDs, we must also consider the local strain within the N-rich regions arising from short-range variations of the lattice constant and/or local distortion. This local strain is mainly uniaxial along the growth direction, judging from the results from the polarization-resolved PL measurements, and is likely to be higher in the areas with higher [N]. Therefore, it should be more important for the low-energy QDs, where combined contributions of the local and global core/shell components give rise to a large LH-HH splitting—see Fig. 5(b), where the total strain in the QDs is shown by the arrows. On the other hand, the contribution of the local strain diminishes in the type-B QDs leading to the observed HH-LH mixing of the VB states.

## VI. CONCLUSIONS

In summary, we employ polarization-resolved and magneto- $\mu$ PL spectroscopy to investigate the electronic structure of the QD states that are formed in the Ga(N, As) shell of GaAs/Ga(N, As) core/shell NWs due to short-range fluctuations in the N composition. Based on the low values of the determined zero-field splitting between the bright states of the confined excitons, the formed QDs are concluded to be of rather high symmetry, though the QD anisotropy seems to be slightly more pronounced for the QDs embedded in the  $\text{GaN}_{0.005}\text{As}_{0.995}$  shell than in the  $\text{GaN}_{0.001}\text{As}_{0.999}$  shell. It is also found that the character of the VB states in the QDs differ for the low- and high-energy emitters, changing from the pure HH character for the former to the mixed LH-HH one for the latter. The observed changes are attributed to the combined effects of the global strain created because of the lattice mismatch between the core and shell materials, and the local strain/lattice distortion within the short-range alloy fluctuations. The resulting strain is concluded to be predominantly uniaxial along the NW axis, to account for the preferential alignment of the quantization axis of the studied QD along the NW growth direction. Our results, therefore, underline the importance of local strain in valence band engineering, which may be utilized for designing hybrid NW structures with embedder QDs for future optoelectronic applications.

## ACKNOWLEDGMENTS

The authors acknowledge the financial support from the Swedish Energy Agency (Grant No. P40119-1) and the Swedish Research Council (Grant No. 2015-05532). I.B. and W.M.C. acknowledge financial support from the Swedish Government Strategic Research Area in Materials Science on Functional Materials at Linköping University (Faculty Grant SFO-Mat-LiU No 2009 00971). The NW growth was partly supported by KAKENHI (Grants No.

16H05970 and No. 23686004) from the Japan Society for the Promotion of Science, research scholarships from the Kato Foundation for Promotion of Science, the Kurata Memorial Hitachi Science and Technology Foundation, and the Murata Science Foundation.

- 
- [1] M. T. Borgstrom, V. Zwiller, E. Muller, and A. Imamoglu, Optically bright quantum dots in single nanowires, *Nano Lett.* **5**, 1439 (2005).
- [2] D. Spirkoska, J. Abriol, A. Gustafsson, S. Conesa-Boj, F. Glas, I. Zardo, M. Heigoldt, M. H. Glass, A. L. Bleloch, S. Estrade, M. Kaniber, J. Rossler, F. Peiro, J. R. Morante, G. Abstreiter, L. Samuelson, and A. Fontcuberta i Morral, Structural and optical properties of high quality zinc-blende/wurtzite GaAs nanowire heterostructures, *Phys. Rev. B* **80**, 245325 (2009).
- [3] M. H. M. van Weert, N. Akopian, U. Perinetti, M. P. van Kouwen, R. E. Algra, M. A. Verheijen, E. P. Bakkers, L. P. Kouwenhoven, and V. Zwiller, Selective excitation and detection of spin states in a single nanowire quantum dot, *Nano Lett.* **9**, 1989 (2009).
- [4] J. Salfi, S. Roddaro, D. Ercolani, L. Sorba, I. Savelev, M. Blumin, H. E. Ruda, and F. Beltram, Electronic properties of quantum dot systems realized in semiconductor nanowires, *Semicond. Sci. Technol.* **25**, 024007 (2010).
- [5] G. Sallen, A. Tribu, T. Aichele, R. André, L. Besombes, C. Bougerol, M. Richard, S. Tatarenko, K. Kheng, and J. Poizat, Subnanosecond spectral diffusion measurement using photon correlation, *Nat. Photonics* **4**, 696 (2010).
- [6] M. Heiss, Y. Fontana, A. Gustafsson, G. Wüst, C. Magen, D. D. O'Regan, J. W. Luo, B. Ketterer, S. Conesa-Boj, A. V. Kuhlmann, J. Houel, E. Russo-Averchi, J. R. Morante, M. Cantoni, N. Marzari, J. Abriol, A. Zunger, R. J. Warburton, and A. Fontcuberta i Morral, Self-assembled quantum dots in a nanowire system for quantum photonics, *Nat. Mater.* **12**, 439 (2013).
- [7] M. A. M. Versteegh, M. E. Reimer, K. D. Jöns, D. Dalacu, P. J. Poole, A. Gulinatti, A. Giudice, and V. Zwiller, Observation of strongly entangled photon pairs from a nanowire quantum dot, *Nat. Commun.* **5**, 5298 (2014).
- [8] M. Weiß, J. B. Kinzel, F. J. R. Schülein, M. Heigl, D. Rudolph, S. Morkötter, M. Döblinger, M. Bichler, G. Abstreiter, J. J. Finley, G. Koblmüller, A. Wixforth, and H. J. Krenner, Dynamic acoustic control of individual optically active quantum dot-like emission centers in heterostructure nanowires, *Nano Lett.* **14**, 2253 (2014).
- [9] B. Loitsch, J. Winnerl, G. Grimaldi, J. Wierzbowski, D. Rudolph, S. Morkötter, M. Döblinger, G. Abstreiter, G. Koblmüller, and J. J. Finley, Crystal phase quantum dots in the ultrathin core of GaAs-AlGaAs core-shell nanowires, *Nano Lett.* **5**, 7544 (2015).
- [10] J. Tatebayashi, S. Kako, J. Ho, Y. Ota, S. Iwamoto, and Y. Arakawa, Room-temperature lasing in a single nanowire with quantum dots, *Nat. Photonics* **9**, 501 (2015).
- [11] A. Davydok, S. Breuer, A. Biermanns, L. Geelhaar, and U. Pietsch, Lattice parameter accommodation between GaAs(111) nanowires and Si(111) substrate after growth via Au-assisted molecular beam epitaxy, *Nanoscale Res. Lett.* **7**, 109 (2012).
- [12] J. Holm, H. I. Jørgensen, P. Krogstrup, J. Nygård, H. Liu, and M. Aagesen, Surface-passivated GaAsP single-nanowire solar cells exceeding 10% efficiency grown on silicon, *Nat. Commun.* **4**, 1498 (2013).
- [13] L. J. Lauhon, M. S. Gudiksen, D. Wang, and C. M. Lieber, Epitaxial core-shell and core-multishell nanowire heterostructures, *Nature* **420**, 57 (2002).
- [14] Y. Wu, R. Fan, and P. Yang, Block-by-block growth of single-crystalline Si/SiGe superlattice nanowires, *Nano Lett.* **2**, 83 (2002).
- [15] N. Jeon, B. Loitsch, S. Morkötter, G. Abstreiter, J. Finley, H. J. Krenner, G. Koblmüller, and L. J. Lauhon, Alloy fluctuations act as quantum dot-like emitters in GaAs-AlGaAs core-shell nanowires, *ACS Nano* **9**, 8335 (2015).
- [16] C. Lü, J. L. Cheng, and M. W. Wu, Hole spin relaxation in semiconductor quantum dots, *Phys. Rev. B* **71**, 075308 (2005).
- [17] F. Dubin, M. Combescot, G. K. Brennen, and R. Melet, Quantum Control of a Trapped Electron Spin in a Quantum Dot using Photon Polarization, *Phys. Rev. Lett.* **101**, 217403 (2008).
- [18] J. I. Clemente, C. Segarra, and J. Planelles, Spin-orbit-induced hole spin relaxation in InAs and GaAs quantum dots, *New J. Phys.* **15**, 093009 (2013).
- [19] M. Jeannin, A. Artioli, P. Rueda-Fonseca, E. Bellet-Amalric, K. Kheng, R. André, S. Tatarenko, J. Cibert, D. Ferrand, and G. Nogues, Light-hole exciton in a nanowire quantum dot, *Phys. Rev. B* **95**, 035305 (2017).
- [20] S. Filippov, M. Jansson, J. E. Stehr, J. Palisaitis, POÅ Persson, F. Ishikawa, W. M. Chen, and I. A. Buyanova, Strongly polarized quantum-dot-like light emitters embedded in GaAs/GaNAs core/shell nanowires, *Nanoscale* **8**, 15939 (2016).
- [21] For a review of dilute nitrides, see e.g. *Physics and Applications of Dilute Nitrides*, edited by I. A. Buyanova and W. M. Chen (Taylor & Francis, New York, 2004).
- [22] N. Tansu, N. J. Kirsch, and L. J. Mawst, Low-threshold-current-density 1300-nm dilute-nitride quantum well lasers, *Appl. Phys. Lett.* **81**, 2523 (2002).
- [23] Z. C. Niu, S. Y. Zhang, H. Q. Ni, D. H. Wu, H. Zhao, H. L. Peng, Y. Q. Xu, S. Y. Li, Z. H. He, Z. W. Ren, Q. Han, X. H. Yang, Y. Du, and R. H. Wu, GaAs-based room-temperature continuous-wave 1.59 μm GaInNAsSb single-quantum-well laser diode grown by molecular-beam epitaxy, *Appl. Phys. Lett.* **87**, 231121 (2005).
- [24] H. Jussila, P. Kivisaari, J. Lemettinen, T. Tanaka, and M. Sopanen, Two-Photon Absorption in GaAs<sub>1-x-y</sub>P<sub>y</sub>N<sub>x</sub> Intermediate-Band Solar Cells, *Phys. Rev. Appl.* **3**, 054007 (2015).
- [25] Y. J. Kuang, K. M. Yu, R. Kudrawiec, A. V. Luce, M. Ting, W. Walukiewicz, and C. W. Tu, GaNAsP: An intermediate band semiconductor grown by gas-source molecular beam epitaxy, *Appl. Phys. Lett.* **102**, 112105 (2013).
- [26] X. J. Wang, I. A. Buyanova, F. Zhao, D. Lagarde, A. Balocchi, X. Marie, C. W. Tu, J. C. Harmand, and W. M. Chen, Room-temperature defect-engineered spin filter based on a non-magnetic semiconductor, *Nat. Mater.* **8**, 198 (2009).

- [27] Y. Puttisong, I. A. Buyanova, A. J. Ptak, C. W. Tu, L. Geelhaar, H. Reichert, and W. M. Chen, Room-temperature electron spin amplifier based on Ga(In)NAs alloys, *Adv. Mater.* **25**, 738 (2013).
- [28] Y. Puttisong, X. J. Wang, I. A. Buyanova, L. Geelhaar, H. Reichert, A. J. Ptak, C. W. Tu, and W. M. Chen, Efficient room-temperature nuclear spin hyperpolarization of a defect atom in a semiconductor, *Nat. Commun.* **4**, 1751 (2013).
- [29] Y. Araki, M. Yamaguchi, and F. Ishikawa, Growth of dilute nitride GaAsN/GaAs heterostructure nanowires on Si substrates, *Nanotechnology* **24**, 065601 (2013).
- [30] S. L. Chen, S. Filippov, F. Ishikawa, W. M. Chen, and I. A. Buyanova, Origin of radiative recombination and manifestations of localized effects in GaAs/GaNAs core/shell nanowires, *Appl. Phys. Lett.* **105**, 253106 (2014).
- [31] W. Shan, W. Walukiewicz, J. W. Ager III, E. E. Haller, J. F. Geisz, D. J. Friedman, J. M. Olson, and S. R. Kurtz, Band Anticrossing in GaInNAs Alloys, *Phys. Rev. Lett.* **82**, 1221 (1999).
- [32] S. L. Chen, M. Jansson, S. Filippov, F. Ishikawa, W. M. Chen, and I. A. Buyanova, Core-shell carrier and exciton transfer in GaAs/GaNAs coaxial nanowires, *J. Vac. Sci. Technol. B* **34**, 04J104 (2016).
- [33] H. E. Ruda and A. Shik, Polarization-sensitive optical phenomena in thick semiconducting nanowires, *J. Appl. Phys.* **100**, 024314 (2006).
- [34] G. Grzela, R. Paniagua-Domínguez, T. Barten, Y. Fontana, J. A. Sánchez-Gil, and J. G. Rivas, Nanowire antenna emission, *Nano Lett.* **12**, 5481 (2012).
- [35] P. Corfdir, F. Feix, J. K. Zettler, S. Fernández-Garrido, and O. Brandt, Importance of the dielectric contrast for the polarization of excitonic transitions in single GaN nanowires, *New J. Phys.* **17**, 033040 (2015).
- [36] G. E. Pikus and G. L. Bir, *Symmetry and Strain Induced Effects in Semiconductors* (Wiley, New York, 1974).
- [37] J. D. Plumhof, R. Trotta, V. Krápek, E. Zallo, P. Atkinson, S. Kumar, A. Rastelli, and O. G. Schmidt, Tuning of the Valence Band Mixing of Excitons Confined in GaAs/AlGaAs Quantum Dots via Piezoelectric-Induced Anisotropic Strain, *Phys. Rev. Lett.* **87**, 075311 (2013).
- [38] C. Tonin, R. Hostein, V. Voliotis, R. Grousson, A. Lemaitre, and A. Martinez, Polarization properties of excitonic qubits in single self-assembled quantum dots, *Phys. Rev. B* **85**, 155303 (2012).
- [39] Y. Léger, L. Besombes, L. Maingault, and H. Mariette, Valence-band mixing in neutral, charged, and Mn-doped self-assembled quantum dots, *Phys. Rev. B* **76**, 045331 (2007).
- [40] S. Ohno, S. Adachi, R. Kaji, S. Muto, and H. Sasakura, Optical anisotropy and photoluminescence polarization in single InAlAs quantum dots, *Appl. Phys. Lett.* **98**, 161912 (2011).
- [41] H. W. van Kesteren, E. C. Cosman, W. A. J. A. van der Poel, and C. T. Foxon, Fine structure of excitons in type-II GaAs/AlGaAs quantum dots, *Phys. Rev. B* **41**, 5283 (1990).
- [42] Q. X. Zhao and B. Monemar, Electronic structure of the substitutional nitrogen NN<sub>1</sub> pair in GaP from photoluminescence excitation and Zeeman spectroscopy, *Phys. Rev. B* **38**, 1397 (1998).
- [43] See Supplemental Material at <http://link.aps.org/supplemental/10.1103/PhysRevApplied.10.044040> for more details about the effective Hamiltonian for the exciton, effects of the core-shell strain on exciton states, spectral dependence of the hole-character and effects of twin-planes, magneto-optical properties of the QD emitters in the GaN<sub>0.005</sub>As<sub>0.995</sub>-based NWs, calculation of the thermal activation energy.
- [44] V. D. Kulakovskii, G. Bacher, R. Weigand, T. Kümmell, A. Forchel, E. Borovitskaya, K. Leonardi, and D. Hommel, Fine Structure of Biexciton Emission in Symmetric and Asymmetric CdSe/ZnSe Single Quantum Dots, *Phys. Rev. Lett.* **82**, 1780 (1999).
- [45] J. Puls, M. Rabe, H.-J. Wünsche, and F. Henneberger, Magneto-optical study of the exciton fine structure in self-assembled CdSe quantum dots, *Phys. Rev. B* **60**, R16303 (1999).
- [46] M. Bayer, O. Stern, A. Kuther, and A. Forchel, Spectroscopic study of dark excitons in In<sub>x</sub>Ga<sub>1-x</sub>As self-assembled quantum dots by a magnetic-field-induced symmetry breaking, *Phys. Rev. B* **61**, 7273 (2000).
- [47] D. Gammon, A. L. Efros, T. A. Kennedy, M. Rosen, D. S. Katzer, D. Park, S. W. Brown, V. L. Korenev, and I. A. Merkulov, Electron and Nuclear Spin Interactions in the Optical Spectra of Single GaAs Quantum Dots, *Phys. Rev. Lett.* **86**, 5176 (2001).
- [48] D. Gammon, E. S. Snow, B. V. Shanabrook, D. S. Katzer, and D. Park, Fine Structure Splitting in the Optical Spectra of Single GaAs Quantum Dots, *Phys. Rev. Lett.* **76**, 3005 (1996).
- [49] M. Bayer, A. Kuther, A. Forchel, A. Gorbunov, V. B. Timofeev, F. Schäfer, J. P. Reithmaier, T. L. Reinecke, and S. N. Walck, Electron and Hole g Factors and Exchange Interaction from Studies of the Exciton Fine Structure in In<sub>0.60</sub>Ga<sub>0.40</sub>As Quantum Dots, *Phys. Rev. Lett.* **82**, 1748 (1999).
- [50] J. J. Finley, D. J. Mowbray, M. S. Skolnick, A. D. Ashmore, C. Baker, A. F. Monte, and M. Hopkinson, Fine structure of charged and neutral excitons in InAs-Al<sub>0.6</sub>Ga<sub>0.4</sub>As quantum dots, *Phys. Rev. B* **66**, 153316 (2002).
- [51] R. Seguin, A. Schliwa, S. Rodt, K. Pötschke, and U. W. Pohl, and D. Bimberg, Size-Dependent Fine-Structure-Splitting in Self-Organized InAs/GaAs Quantum Dots, *Phys. Rev. Lett.* **95**, 257402 (2005).
- [52] M. Abbarchi, T. Kuroda, C. Mastrandrea, A. Vinattieri, S. Sanguinetti, T. Mano, K. Sakoda, and M. Gurioli, Fine structure splitting of quantum dot excitons: Role of geometry and environment, *Physica E* **42**, 881 (2010).
- [53] A. Schliwa, M. Winkelkemper, A. Lochmann, E. Stock, and D. Bimberg, In(Ga)As/GaAs quantum dots grown on a (111) surface as ideal sources of entangled photon pairs, *Phys. Rev. B* **80**, 161307 (2009).
- [54] E. Stock, T. Warming, I. Ostapenko, S. Rodt, A. Schliwa, J. A. Töfflinger, A. Lochmann, A. I. Toropov, S. A. Moshchenko, D. V. Dmitrev, V. A. Haisler, and D. Bimberg, Single-photon emission from InGaAs quantum dots grown on (111) GaAs, *Appl. Phys. Lett.* **96**, 093112 (2010).
- [55] J. Treu, C. Schneider, A. Huggenberger, T. Braun, S. Reitzenstein, S. Höfling, and M. Kamp, Substrate orientation dependent fine structure splitting of symmetric In(Ga)As/GaAs quantum dots, *Appl. Phys. Lett.* **101**, 022102 (2012).

- [56] C. D. Yerino, P. J. Simmonds, B. Liang, D. Jung, C. Schneider, S. Unsleber, M. Vo, D. L. Huffaker, S. Höfling, M. Kamp, and L. M. Lee, Strain-driven growth of GaAs(111) quantum dots with low fine structure splitting, *Appl. Phys. Lett.* **105**, 251901 (2014).
- [57] J. M. Luttinger, Quantum theory of cyclotron resonance in semiconductors: General theory, *Phys. Rev.* **102**, 1030 (1956).
- [58] G. Pettinari, F. Masia, A. Polimeni, M. Felici, A. Frova, M. Capizzi, A. Lindsay, E. P. O'Reilly, P. J. Klar, W. Stolz, G. Bais, M. Piccin, S. Rubini, F. Martelli, and A. Franciosi, Influence of nitrogen-cluster states on the gyromagnetic factor of electrons in  $\text{GaAs}_{1-x}\text{N}_x$ , *Phys. Rev. B* **74**, 245202 (2006).
- [59] S. N. Walck and T. L. Reinecke, Exciton diamagnetic shift in semiconductor nanostructures, *Phys. Rev. B* **57**, 9088 (1998).
- [60] F. Masia, G. Pettinari, A. Polimeni, M. Felici, A. Miriametro, M. Capizzi, A. Lindsay, S. B. Healy, E. P. O'Reilly, A. Cristofoli, G. Bais, M. Piccin, S. Rubini, F. Martelli, A. Franciosi, P. J. Klar, K. Volz, and W. Stolz, Interaction between conduction band edge and nitrogen states probed by carrier effective-mass measurements in  $\text{GaAs}_{1-x}\text{N}_x$ , *Phys. Rev. B* **73**, 073201 (2006).
- [61] P. D. Wang, J. L. Merz, S. Fafard, R. Leon, D. Leonard, G. Medeiros-Ribeiro, M. Oestreich, P. M. Petroff, K. Uchida, N. Miura, H. Akiyama, and H. Sakaki, Magnetoluminescence studies of  $\text{In}_y\text{As}_{1-y}\text{As}$  self-assembled quantum dots in  $\text{Al}_x\text{Ga}_{1-x}\text{As}$  matrices, *Phys. Rev. B* **53**, 16458 (1996).
- [62] P. D. Wang, J. L. Merz, S. Fafard, R. Leon, D. Leonard, G. Medeiros-Ribeiro, M. Oestreich, P. M. Petroff, N. N. Ledentsov, P. S. Kop'ev, V. M. Ustinov, K. Uchida, N. Miura, H. Akiyama, H. Sakaki, and C. M. Sotomayor Torres, Magneto-optical properties of InAs monolayers and  $\text{In}_y\text{Al}_{1-y}\text{As}$  self-assembled quantum dots in  $\text{Ga}(\text{Al})\text{As}$  matrices, *Physica B* **227**, 378 (1996).
- [63] A. M. Mintairov, T. H. Kosel, J. L. Merz, P. A. Blagnov, A. S. Vlasov, V. M. Ustinov, and R. E. Cook, Near-Field Magnetoluminescence Spectroscopy of Composition Fluctuations in  $\text{InGaAsN}$ , *Phys. Rev. Lett.* **87**, 277401 (2001).
- [64] A. M. Mintairov, P. A. Blagnov, J. L. Merz, V. M. Ustinov, A. S. Vlasov, A. R. Kovsh, J. S. Wang, L. Wei, and J. Y. Chi, Near-field magneto-photoluminescence of quantum-dot-like composition fluctuations in  $\text{GaAsN}$  and  $\text{InGaAsN}$  alloys, *Physica E* **21**, 385 (2004).
- [65] D. Ferrand and J. Cibert, Strain in crystalline core-shell nanowires, *Eur. Phys. J. Appl. Phys.* **67**, 30403 (2014).
- [66] M. Montazeri, M. Fickenscher, L. M. Smith, H. E. Jackson, J. Yarrison-Rice, J. H. Kang, Q. Gao, H. H. Tan, C. Jagadish, Y. Guo, J. Zou, M.-E. Pistol, and C. E. Pryor, Direct measure of strain and electronic structure in  $\text{GaAs}/\text{GaP}$  core-shell nanowires, *Nano Lett.* **10**, 880 (2010).
- [67] P. Stepanov, M. Elzo-Aizarna, J. Bleuse, N. S. Malik, Y. Curé, E. Gautier, V. Favre-Nicolin, J.-M. Gérard, and J. Claudon, Large and uniform optical emission shifts in quantum dots strained along their growth axis, *Nano Lett.* **16**, 3215 (2016).
- [68] I. Vurgaftman, J. R. Meyer, and L. R. Ram-Mohan, Band parameters for III-V compound semiconuductors and their alloys, *Appl. Phys. Rev.* **89**, 5815 (2001).

*Correction:* In several locations in Sec. IV, the  $x$ ,  $y$ , and  $z$  directions were given incorrectly and have been fixed. A missing minus sign in Eq. (2) has been inserted. Some values of  $\gamma$  in Table I were improperly placed during production and have been rectified.